

Design Optimisation and Control of Compliant Actuation Arrangements in Articulated Robots for Improved Energy Efficiency

Wesley Roozing, Zhibin Li, Darwin G. Caldwell, and Nikos G. Tsagarakis

Abstract—The development of energy efficient actuation represents one of the biggest challenges in robotics research today. This letter presents the generalisation of design and control concepts for a recently introduced asymmetric compliant actuator, as well as its extension to multi-DoF articulated robotic systems. The actuator design consists of two actuation branches with significantly different stiffness and energy storage capacity properties driving a single joint. The letter studies and presents a novel method to select the design parameters of asymmetric compliant actuation schemes to improve the energy efficiency of multi-DoF articulated robots powered by this type of actuators. An optimisation problem is formulated to optimise the actuation parameters for energy efficient operation. Simulation studies performed on a 2-DoF leg as proof-of-concept demonstrate significant improvements in electrical energy efficiency and reduction in peak torque and electrical power requirements. Furthermore, biarticulated actuation arrangements are also investigated, and they are proven to further enhance the energy efficiency of the robotic leg.

Index Terms—Compliant Joint/Mechanism, Force Control.

I. INTRODUCTION

AS robot applications have expanded from static industrial domains to motion/locomotion based service sectors there have been increased performance needs that impact a number of aspects of robot design. Among the most pressing has been the development of high-performance, energy efficient actuators. One important feature that has received noteworthy attention is actuation systems that include compliant elements which can be used for energy storage. As in biological systems, the use of compliant actuation can improve energy efficiency [1]–[4], force regulation [6]–[8], and peak output power characteristics [5]. Moreover, the addition of compliance has the potential to increase physical robustness, interaction safety [9]–[11], and protection of the actuators themselves. Compliance can also compensate for gravitational loading, e.g. by placing compliant elements in parallel with the primary drive. This can result in improved energy efficiency [12]. Recently, several compliant actuators have been developed, ranging from Series-Elastic Actuators (SEAs) with

fixed compliance [6]–[8], [13] to Variable Stiffness Actuators (VSAs) [1]–[3], [5], [9], [11], [14]–[18].

In biological systems, biarticulated muscle structures, where a single muscle spans multiple joints, are common. This principle has been used as a basis for biarticulated robotic actuators, where it has been shown to increase the force regulation, energy efficiency and peak power properties of both biological [19], [20] and robotic systems [21]–[25].

One area that could particularly benefit from high performance, energy efficient, compliant actuation is legged robotics. However, to date, compliant actuators have not commonly demonstrated energy efficiency benefits on real-world systems. This is because the design and control of such actuators is not sufficiently well understood.

An alternative mechanical structure that aims to substantially improve efficiency is the asymmetric compliant actuator (ACA) [26]–[28] which combines a high power motion branch with an energy storage branch. In [28] a novel distributed controller was developed using both branches of this ACA for energy efficient operation. The authors experimentally verified the potential of mechanism and controller on a 1-DoF leg demonstrating a 65% reduction in electrical power consumption when compared to conventional SEA.

This letter significantly extends these previous works and contributes by:

- Generalising the design and control concepts of asymmetric compliant actuation to multi-DoF systems;
- Extending asymmetric compliant actuation principle to biarticulated actuation structures;
- Proposing a novel method for optimizing the parameters of these multi-DoF asymmetric compliant actuation configurations to improve their energy efficiency.

These extensions and generalisations provide the necessary guidelines for future development of more complex systems and, ultimately, integration on humanoids such as WALK-MAN [29]. Most existing humanoids and many other robotic systems employ stiff or conventional series-elastic actuation. Thus, we use SEA as the basis for comparison against our methods. The results of these comparative studies demonstrate significant energy efficiency benefits when using ACA for multi-DoF robotic systems. Indeed, we believe that the ACA concept can improve the energy efficiency and power autonomy of many robotic platforms.

The letter is structured as follows. Section II describes the asymmetric actuation, biarticulated actuation, and a 2-DoF

Manuscript received August 31, 2015; accepted January 8, 2016. Date of publication January 26, 2016; date of current version March 18, 2016. This paper was recommended for publication by Associate Editor L. Zhang and Editor J. Li upon evaluation of the reviewers comments. This work is supported by the WALK-MAN FP7-ICT 611832 European Commission project.

The authors are with the Department of Advanced Robotics, (Fondazione) Istituto Italiano di Tecnologia, Genova 16163, Italy (e-mail: wesley.roozing@iit.it; zhibin.li@iit.it; darwin.caldwell@iit.it; nikos.tsagarakis@iit.it).

Digital Object Identifier 10.1109/LRA.2016.2521926

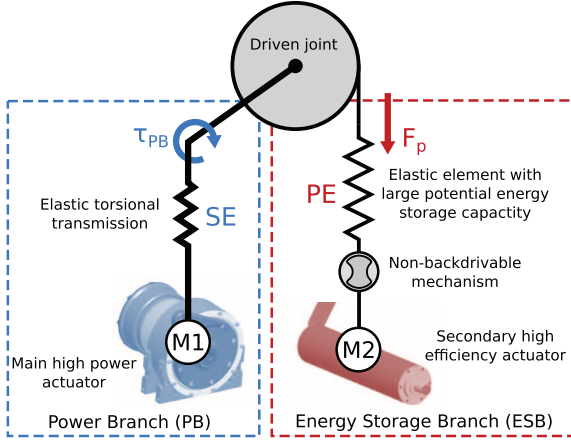


Fig. 1. Asymmetric compliant actuation concept.

proof-of-concept leg model used to demonstrate the effectiveness of our methods. Furthermore, the models are formulated. Section III discusses the methods used for optimisation of the actuation design parameters for general multi-DoF systems, actuated by an arbitrary combination of mono- and biarticulated actuators. Section IV presents the control architecture for multi-DoF systems. A simulation study is presented and data are analysed in Section V, followed by conclusions and suggestions for future work in Section VI.

II. ASYMMETRIC COMPLIANT ACTUATION CONCEPT

The components of the ACA concept are shown in Fig. 1. The joint is driven by two parallel actuation branches with very different power and stiffness properties.

The Power Branch (PB) is a rotary series elastic actuator that consists of a high power motor $M1$ in series with a torsional elastic element SE . The Energy Storage Branch (ESB) consists of a lower power motor $M2$ with a high reduction linear transmission. The motor transfers its power to the joint through a unidirectional series elastic element PE . The main characteristics of the elastic element are a lower stiffness and very large energy storage capacity. More details on the concept and a 1-DoF hardware implementation can be found in [26]–[28].

A. Biarticulated Actuation Structures

In contrast to most existing robots, humans utilise biarticulated muscle structures that actuate multiple joints with a single muscle. Examples include the hamstrings, which span both the hip and knee joints, and the gastrocnemius muscle that spans both the knee and ankle joints. Fig. 2 shows the actuation concept of Fig. 1 in biarticulated configuration. The PB drives the joint directly, but the ESB tendon spans the right joint via a free pulley and then drives the left joint.

As a result, the extension of elastic element PE is dependent on the configuration of both joints, and the tendon produces a torque on both joints. Selection of the pulley radii ratio allows to shape the torque profile as a function of both joint positions instead of one joint position.

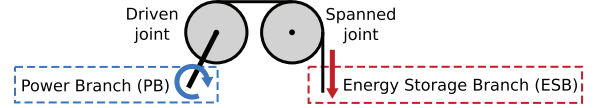


Fig. 2. Actuation concept - Biarticulated configuration.

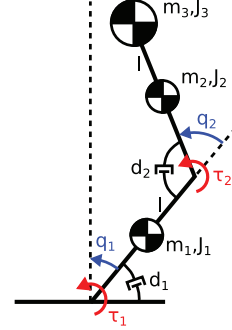


Fig. 3. 2-DoF leg model.

B. 2-DoF Leg

As a proof-of-concept to demonstrate the effectiveness of our methods, we consider a 2-DoF leg model with properties similar to our 1-DoF prototype in [26]–[28]. Both DoFs are actuated and experience viscous friction. We consider the foot to be in good contact, so that it can be considered fixed.

C. Dynamics Modelling

In the following, we opted for a modular modelling approach, for simulation purposes: this allows to quickly test a variety of actuation arrangements.

1) *Leg Modelling*: The leg model (Fig. 3) consists of two links of length l , mass m_1, m_2 , and rotational inertiae J_1, J_2 , connected by an actuated knee joint. On the hip there is a load mass m_3 with rotational inertia J_3 . The lower link pivots around the ground contact through the actuated ankle joint, resulting in a 2-DoF system with 2 inputs. Both joints are damped by viscous friction with coefficients d_1, d_2 . The dynamics of this model are described by

$$\ddot{\mathbf{q}} = \mathbf{M}(\mathbf{q})^{-1} [\boldsymbol{\tau} + \mathbf{G}(\mathbf{q}) - \mathbf{D}\dot{\mathbf{q}}] \quad (1)$$

where $[q_1, q_2]^T =: \mathbf{q} \in \mathcal{Q} \subseteq \mathbb{R}^2$ denotes the configuration variables as in Fig. 3, $\boldsymbol{\tau} \in \mathbb{R}^2$ denotes the actuator torques, the damping matrix $\mathbf{D} = \text{diag}(d_1, d_2)$ denotes joint friction, and $\mathbf{G}(\mathbf{q}) \in \mathbb{R}^2$ denotes the generalised gravitational torque:

$$\mathbf{G}(\mathbf{q}) = \mathbf{J}(\mathbf{q})^T \mathbf{G}_c \quad (2)$$

where $\mathbf{J}(\mathbf{q})$ denotes the system Jacobian and the gravitation vector \mathbf{G}_c is given by

$$\mathbf{G}_c = [0, -m_1g, 0, 0, -m_2g, 0, 0, -m_3g, 0]^T \quad (3)$$

and $g = 9.81 \text{ m/s}^2$. In all notation, $\dot{[\cdot]}$ denotes the time derivative and $[\cdot]^T$ denotes the transpose. We ignore the centripetal and Coriolis forces. The generalised inertia matrix $\mathbf{M}(\mathbf{q}) \in \mathbb{R}^{N \times N}$ is given by

$$\mathbf{M}(\mathbf{q}) = \mathbf{J}^T(\mathbf{q}) \mathbf{M}_c \mathbf{J}(\mathbf{q}) \quad (4)$$

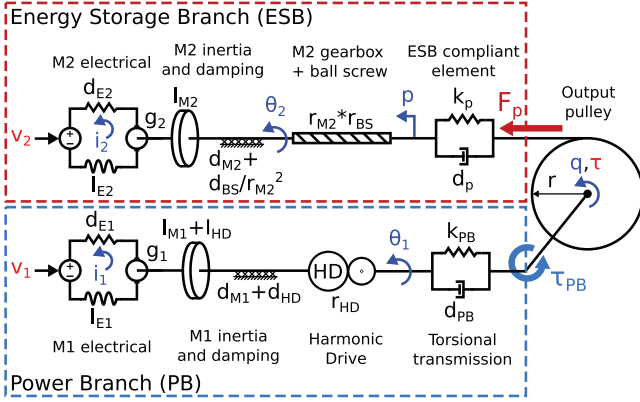


Fig. 4. Actuator model - Monoarticulated configuration.

with the nominal inertia matrix M_c defined as

$$M_c = \text{diag}(m_1, m_1, J_1, m_2, m_2, J_2, m_3, m_3, J_3). \quad (5)$$

2) *Actuator Modelling*: The actuator model is shown in Fig. 4. We include electrical dynamics of motors $M1$ and $M2$, in which $I_{E1}, I_{E2}, d_{E1}, d_{E2}$ denote winding induction and resistances respectively. The motor currents are denoted as i_1, i_2 and the torque constants are denoted as g_1, g_2 .

In the mechanical domain, the lumped $M1$ inertia and damping are denoted as $I_{M1} + I_{HD}$ and $d_{M1} + d_{HD}$ respectively. The Harmonic Drive transmission ratio is denoted as r_{HD} . The torsional transmission bar is modelled as a spring-damper with stiffness k_{PB} and damping d_{PB} , such that the PB torque on the knee joint τ_{PB} is given by

$$\tau_{PB} = k_{PB}\Delta L_{PB} + d_{PB}\Delta \dot{L}_{PB} \quad (6)$$

where $\Delta L_{PB} = \theta_1 - q$ denotes the deflection of the torsional transmission of the Power Branch.

The $M2$ rotor inertia is denoted as I_{M2} , and the ball screw inertia is neglected. The reflected damping of $M2$ and ball screw is denoted as $d_{M2} + d_{BS}/r_{M2}^2$, where r_{M2} denotes the gearbox ratio. The ball screw transmission ratio is r_{BS} .

Since the elastic element PE is a rubber type material, it only applies elastic force under extension. Therefore the element is modelled as a unidirectional spring-damper:

$$F_p = \begin{cases} k_p \Delta L_p + d_p \Delta \dot{L}_p & \Delta L_p > 0 \\ d_p \Delta \dot{L}_p & \text{otherwise} \end{cases} \quad (7)$$

where k_p denotes the spring constant, d_p denotes the damping and ΔL_p denotes the spring extension $\Delta L_p = p - r q$. The pretension position p is set by motor $M2$ as $p = \eta_1^{-1} \theta_2$ where $\eta_1 = r_{M2} r_{BS}$. The torque generated by the ESB on the joint is then given by $\tau_p = r F_p$, where r denotes the output pulley radius. The net joint torque τ is given by the sum of contributions of PB and ESB : $\tau = \tau_{PB} + \tau_p$.

The actuator dynamics are written as a set of first-order coupled differential equations:

$$\dot{\mathbf{x}} = \mathbf{f}(\mathbf{x}) + \mathbf{g}(\mathbf{u}) \quad (8)$$

where the state \mathbf{x} is defined as

$$\mathbf{x} = [i_1, i_2, \dot{\theta}_1, \dot{\theta}_2, \Delta L_{PB}, \Delta L_p, \theta_1, \theta_2]^T \quad (9)$$

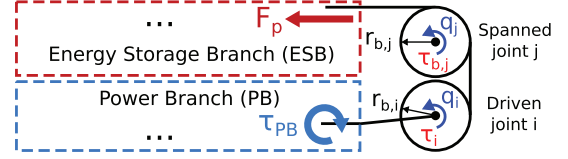


Fig. 5. Actuator model - Biarticulated configuration driving joint i with the ESB tendon spanning joint j .

where $\dot{\theta}_1, \dot{\theta}_2, \theta_1, \theta_2$ denote the motor velocities and positions in Fig. 4. The input vector \mathbf{u} is defined as

$$\mathbf{u} = [v_1, v_2, \dot{q}]^T \quad (10)$$

where v_1, v_2 denote the motor input voltages and \dot{q} denotes the joint velocity.

3) *Biarticulated Configurations*: The biarticulated configuration of the actuator model is shown in Fig. 5, where joint i is driven and the ESB tendon spans joint j . In this case the elongation of the ESB elastic element is given by both joints:

$$\Delta L_p = p - r_{b,i} q_i - r_{b,j} q_j \quad (11)$$

and the tendon generates torque on both joints. The input vector (10) becomes $\mathbf{u} = [v_1, v_2, \dot{\mathbf{q}}_b]^T$ where $\dot{\mathbf{q}}_b = [\dot{q}_i, \dot{q}_j]$ denotes the vector of joint velocities. The net joint torques in biarticulated configuration are given by:

$$\begin{aligned} \tau_i &= \tau_{b,i} + \tau_{PB,i} \\ \tau_j &= \tau_{b,j} \end{aligned} \quad (12)$$

where the ESB torques are $\tau_{b,i} = r_{b,i} F_p$ and $\tau_{b,j} = r_{b,j} F_p$, and $\tau_{PB,i}$ denotes the PB torque on the driven joint i .

III. OPTIMISATION OF DESIGN PARAMETERS

This section introduces an optimisation method to select the design parameters of the Energy Storage Branches. Based on the gravitational load, stiffness, and inertial properties, the actuation parameters can be chosen such that the $ESBs$ provide maximum load compensation for higher energy efficiency and reduction of peak torque/power requirements.

By considering pulley radii, elastic element stiffnesses and pretension positions, we introduce an optimisation procedure that maximises compensation torque provided by the $ESBs$ over the N-DoF workspace. We first describe a reduction of the number of parameters for the mono- and biarticulated actuation cases. Next we elaborate on the actuation configurations and introduce optimisation problem. This section concludes with results for the leg actuation configurations.

A. Monoarticulated Joints

Assuming low velocity movements of the leg, the damping of the elastic element PE can be neglected and its torque written in the following linear form for the monoarticulated case:

$$\tau_m = \varphi_1 + \varphi_2 q \quad (13)$$

where τ_m denotes monoarticulated ESB torque and $\varphi_1 = -r k_p p$ and $\varphi_2 = -r^2 k_p$. Given optimal values $\varphi_{1,opt}$ and

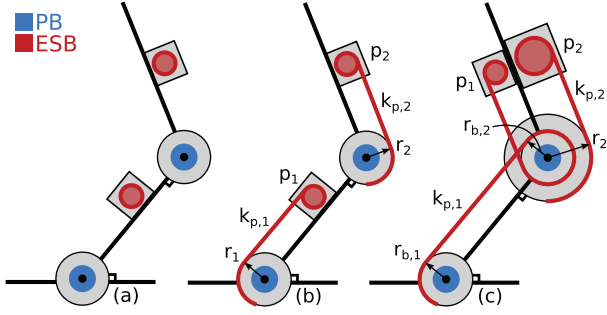


Fig. 6. Leg actuation configurations: SEA (a), mono- (b) and biarticulated (c). In (b), ankle and knee are monoarticulated. In (c), the biarticulated *ESB* spans the knee and ankle joints.

$\varphi_{2,opt}$, then k_p and p can be parametrised with respect to a chosen pulley radius r :

$$k_p(r) = \frac{\varphi_{2,opt}}{r^2} \quad p(r) = r \frac{\varphi_{1,opt}}{\varphi_{2,opt}}. \quad (14)$$

Hence, the number of parameters for this monoarticulated *ESB* is reduced from 3 to 2.

B. Biarticulated Joints

Similarly to the monoarticulated case, the biarticulated *ESB* torque $\tau_{b,i}, \tau_{b,j}$ generated on joints i and j (Fig. 5) can be written as

$$\begin{aligned} \tau_{b,i} &= \varphi_3 \varphi_5 - \varphi_3^2 q_i - \varphi_3 \varphi_4 q_j, \\ \tau_{b,j} &= \varphi_4 \varphi_5 - \varphi_3 \varphi_4 q_i - \varphi_4^2 q_j, \end{aligned} \quad (15)$$

where $\varphi_3 = \sqrt{k_p r_{b,i}}$, $\varphi_4 = \sqrt{k_p r_{b,j}}$, and $\varphi_5 = \sqrt{k_p} p$. Given optimal values $\varphi_{1,opt}$, $\varphi_{2,opt}$ and $\varphi_{3,opt}$, then $r_{b,i}$, k_p and p can be parametrised with respect to a chosen value of the driven joint pulley radius $r_{b,i}$:

$$\begin{aligned} k_p(r_{b,i}) &= \left(\frac{\varphi_{3,opt}}{r_{b,i}} \right)^2, \quad r_{b,j}(r_{b,i}) = \frac{\varphi_{4,opt}}{\sqrt{k_p}}, \\ p(r_{b,i}) &= \frac{\varphi_{5,opt}}{\sqrt{k_p}}. \end{aligned} \quad (16)$$

Similarly, the number of parameters of the biarticulated *ESB* is reduced from 4 to 3.

C. 2-DoF Leg Actuation Configurations

We consider three actuator configurations for the 2-DoF leg, shown in Fig. 6. In Fig. 6a, we consider both joints to be actuated by only the Power Branch, i.e. with the *ESB* removed, resulting in a conventional SEA system.

Shown in Fig. 6b is the second configuration, in which both joints are driven by a *PB* and a monoarticulated *ESB*, as in Fig. 1. The *ESB* torques $\tau_p = [\tau_{p,1}, \tau_{p,2}]^T$ on the joints are given by

$$\begin{bmatrix} \tau_{p,1} \\ \tau_{p,2} \end{bmatrix} = \begin{bmatrix} \tau_{m,1} \\ \tau_{m,2} \end{bmatrix}. \quad (17)$$

There are 6 parameters for the *ESB* branches: the pulley radii r_1, r_2 , stiffnesses $k_{p,1}, k_{p,2}$, and pretension positions p_1, p_2 . Following Sec. III-A, these can be rewritten into 4 parameters as $\varphi = [\varphi_1, \varphi_2, \varphi_3, \varphi_4]$ where φ_1, φ_2 describe the ankle *ESB* and φ_3, φ_4 describe the knee *ESB*.

Shown in Fig. 6c is the third configuration, in which the knee joint is actuated by a *PB* and a monoarticulated *ESB*, and the ankle is actuated by a *PB* and a biarticulated *ESB* which spans both the knee and ankle joint, as in Fig. 5. This configuration is equal to the gastrocnemius muscle in humans, which connects the hip bone to the heel bone, spanning both the knee and ankle joints. This configuration was chosen because it allows a power transfer from knee extension to foot push-off, thus aiding in squatting motions and providing increased foot push-off power during walking, running and jumping. The *ESB* torques are given by

$$\begin{bmatrix} \tau_{p,1} \\ \tau_{p,2} \end{bmatrix} = \begin{bmatrix} \tau_{b,1} \\ \tau_{b,2} \end{bmatrix} + \begin{bmatrix} 0 \\ \tau_m \end{bmatrix}. \quad (18)$$

Due to the additional free pulley required for spanning the knee joint, there are 7 *ESB* parameters in this configuration: the pulley radii $r_{b,1}, r_{b,2}, r_2$, stiffnesses $k_{p,1}, k_{p,2}$ and pretension positions p_1, p_2 . Using Sec. III-A and III-B, these can be rewritten into 5 parameters as $\varphi = [\varphi_1, \varphi_2, \varphi_3, \varphi_4, \varphi_5]$ where $\varphi_1, \varphi_2, \varphi_3$ describe the biarticulated *ESB* and φ_4, φ_5 describe the monoarticulated *ESB*.

The conventional SEA configuration does not require any *ESB* parameters. In the other two cases, we would like to find the value of φ that minimises the error between the *ESB* torques and some desired torque functions over a subset of the workspace of the leg. In the next section, we proceed to formulate this optimisation problem.

D. Optimisation Problem

To optimise the *ESB* parameter vector φ , we first define the error vector $\mathbf{e}(\mathbf{q}) \in \mathbb{R}^N$ for N joints as

$$\mathbf{e} = \boldsymbol{\zeta}(\mathbf{q}) + \boldsymbol{\tau}_p(\mathbf{q}) \quad (19)$$

where $\boldsymbol{\tau}_p(\mathbf{q})$ denotes the *ESB* torques on the joints, which can be composed of an arbitrary mono- or biarticulated configuration. For simplicity, we consider the system to be fully actuated. The function $\boldsymbol{\zeta}(\mathbf{q})$ denotes the vector of desired torques. Here we shall consider static gravitational joint torque compensation: $\boldsymbol{\zeta}(\mathbf{q}) = \mathbf{G}(\mathbf{q})$. For highly dynamic behaviour known at design time, $\boldsymbol{\zeta}$ may include inertial and damping components for efficient execution of those motions. However, these are outside the scope of this letter.

The total error $E(\varphi) \in \mathbb{R}$ is defined as the integrated l^2 -norm over a subset of the workspace:

$$E(\varphi) = \int_{\mathbf{q} \in \mathcal{Q}_d} \|\lambda \mathbf{e}(\mathbf{q}, \varphi)\|_2 \, d\mathbf{q}, \quad (20)$$

where $\lambda \in \mathbb{R}^{N \times N}$ is a diagonal matrix that allows to weigh some joints more than others (here $\lambda = I$), and $\mathcal{Q}_d \subset \mathcal{Q}$ is a subset of the joint workspace on which to optimise and depends on the specific robot. Using the l^2 -norm approximates minimising the electrical power consumption directly, as the

electrical power of a BLDC motor can be approximated (neglecting electrical dynamics) by its squared torque. An optimal solution φ_{opt} minimises E :

$$\begin{aligned} \varphi_{opt} &= \min_{\varphi} E(\varphi) \\ \text{s.t. } \underline{\varphi} &\leq \varphi \leq \overline{\varphi} \end{aligned} \quad (21)$$

where $\underline{\varphi}$ and $\overline{\varphi}$ denote the lower and upper bounds of φ respectively. Note that due to the redundancy in the original parameters, the choice of the free parameters should be such that the bounds on the original parameters are not violated.

For the cases in Sec. III-C, the globally optimal value can be easily found by choosing realistic initial values and standard optimisation algorithms. However, due to the two (monoarticulated) or three (biarticulated) parameters corresponding to each actuated joint, we have $\dim(\varphi) \geq 2N$ for N joints. Thus, when N becomes large, solving for φ_{opt} by minimising (20) becomes infeasible. However, realising that each parameter affects only one or two (in the biarticulated case) joints, the problem can be partitioned into multiple smaller optimisation problems which are solved for a partition of the complete parameter vector. In the following section we shall discuss the partitioned case.

E. Partitioning

Let $\mathbf{e}^c \subset \mathbf{e}$ denote the subset of errors and $\varphi^c \subset \varphi$ the corresponding parameters of the joints belonging to the partition, where the superscript $[\cdot]^c$ denotes the partitioning. We then define the error for the partition similarly to (20):

$$E^c(\varphi^c) = \int_{\mathbf{q} \in \mathcal{Q}_d} \|\lambda^c \mathbf{e}^c(\mathbf{q}, \varphi^c)\|_2 d\mathbf{q}. \quad (22)$$

Note we are still required to integrate over $\forall \mathbf{q} \in \mathcal{Q}_d$, as even though the actuation is decoupled, the joint load still depends on the configuration of all joints. The parameters in the partition can then be optimised by minimising E^c :

$$\begin{aligned} \varphi_{opt}^c &= \min_{\varphi^c} E^c(\varphi^c) \\ \text{s.t. } \underline{\varphi}^c &\leq \varphi^c \leq \overline{\varphi}^c \end{aligned} \quad (23)$$

where $\underline{\varphi}^c$ and $\overline{\varphi}^c$ denote the lower and upper bounds of the partitioned parameters φ^c respectively.

For the monoarticulated case (shown in Fig. 6b) the problem can be partitioned as $\varphi_1^c = [\varphi_1, \varphi_2]$ and $\varphi_2^c = [\varphi_3, \varphi_4]$, i.e. the parameters of each joint can be optimised separately, reducing the problem to two independent one-dimensional line fitting problems. Hence, using appropriate partitioning, the parameters for structures with many joints can be optimised.

F. 2-DoF Leg Parameters

To select the actuation parameters, we consider that the hip is loaded with an additional 40 kg of weight, simulating the weight of a humanoid robot standing on both legs. To obtain the optimisation workspace \mathcal{Q}_d , we define a mapping from polar coordinates of the hip to the joint variables as $\Gamma: (\beta, r) \rightarrow \mathbf{q}$, where β, r denote the polar angle and radius, chosen $-0.4 \leq$

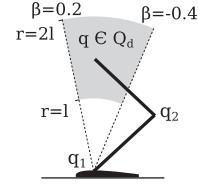


Fig. 7. The workspace subset \mathcal{Q}_d on which the *ESB* actuation parameters are optimised.

TABLE I
OPTIMAL *ESB* PARAMETERS FOR 2-DOF LEG

Monoart.	Value	Biart.	Value
r_1, r_2	0.060 m (chosen)	$r_{b,1}, r_2$	0.060 m (chosen)
$k_{p,1}$	7.69 kN/m	$r_{b,2}$	0.035 m
$k_{p,2}$	16.4 kN/m	$k_{p,1}$	69.4 kN/m
		$k_{p,2}$	14.7 kN/m

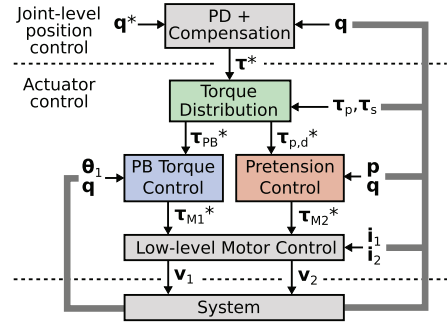


Fig. 8. Control Architecture.

$\beta \leq 0.2$ and $l \leq r \leq 2l$ (Fig. 7), thereby covering the entire feasible workspace of the hip above the stance foot. The optimal parameters are listed in Table I.

IV. CONTROL STRATEGY

The proposed architecture to control the joint variables is shown in Fig. 8. An outer loop tracks position references on the joint variables \mathbf{q} using a PD controller with gravity compensation. The resulting desired joint torques τ^* are given by:

$$\tau^* = -\mathbf{G}(\mathbf{q}) + \mathbf{K}_q [\mathbf{e}_q + \mathbf{D}_q \dot{\mathbf{e}}_q] \quad (24)$$

where $\mathbf{e}_q = \mathbf{q}^* - \mathbf{q} \in \mathbb{R}^N$ denotes the joint variable errors, \mathbf{G} again denotes the gravitational torques and $\mathbf{K}_q, \mathbf{D}_q \in \mathbb{R}^{N \times N}$ denote diagonal control gain matrices. The actuator control, presented next, is designed to be agnostic with respect to the outer control loop. For example, the desired joint torques can also result from advanced whole-body control schemes. Indeed, the actuator control simply tracks the desired joint torques in an energy efficient manner.

In the actuator control strategy, the desired joint torques τ^* are distributed among the *PB* and *ESB* controllers, as shown top left in Fig. 9:

The desired *PB* torques are calculated by subtracting the measured *ESB* torques from the desired joint torques:

$$\tau_{PB}^* = \tau^* - \tau_p.$$

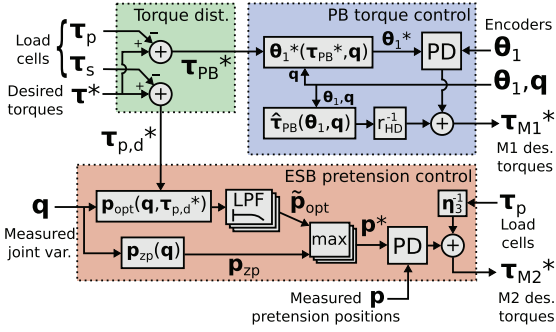


Fig. 9. Reference torque distribution (green), *PB* torque control (blue) and *ESB* pretension control (red).

The desired *ESB* torques are calculated in terms of torque generated on the driven joints as $\tau_{p,d}^*$. We first define τ_s , consisting of the measured torques on spanned joints from biarticulated *ESBs* (e.g. the torque on the knee by the biarticulated *ESB* in Fig. 6c, where $\tau_s = [0, \tau_{b,2}]^T$). We then obtain the desired *ESB* torques as $\tau_{p,d}^* = \tau^* - \tau_s$.

Given the pretension-torque relations for the *ESBs*, it is straightforward to calculate pretension positions \mathbf{p} that achieve desired joint *ESB* torques. However, the resulting pretension positions depend linearly on the joint positions \mathbf{q} , corresponding to a certain elongation of the elastic elements. Since there is unavoidable high-frequency behaviour in the joint variables, this would require high-frequency pretension position control to track the desired torques exactly. This is not desirable behaviour given the relatively low bandwidth and the high transmission ratio of the *ESB* actuation. Hence, we consider a control strategy in which the low-frequency components are tracked, and use the high bandwidth of the *PBs* to ensure the desired joint torques τ^* are achieved by the net torque from both contributions: $\tau_p + \tau_{PB} \approx \tau^*$.

This section will detail the *PB* torque control and *ESB* pretension control strategies. The architecture requires only motor and joint encoders and *ESB* load cell measurements. The resulting desired motor torques τ_{M1}^* and τ_{M2}^* are used as references by low-level motor current controllers.

A. *PB* Torque Control

To achieve desired joint *PB* torques, we exploit the flexible torsional transmission as both a force regulating and measuring element. By controlling the motor-side variables and using a model of the torsional transmission, we achieve link-side torque control. Neglecting the damping, desired *PB* torques τ_{PB} are achieved by motor positions given by:

$$\theta_1^* = K_{PB}^{-1} \tau_{PB}^* + \mathbf{q} \quad (25)$$

where $K_{PB} \in \mathbb{R}^{N \times N}$ denotes the diagonal matrix of *PB* stiffnesses. We then control the *M1* torques using a position control with compensation scheme (blue block in Fig. 9):

$$\tau_{M1}^* = r_{HD}^{-1} \hat{\tau}_{PB} + K_m [\mathbf{e}_m + D_m \dot{\mathbf{e}}_m] \quad (26)$$

where $\mathbf{e}_m = \theta_1^* - \theta_1 \in \mathbb{R}^N$ denotes the motor position errors, and $K_m, D_m \in \mathbb{R}^{N \times N}$ denote diagonal control gain matrices. The compensation term $\hat{\tau}_{PB} \in \mathbb{R}^N$, which is scaled by

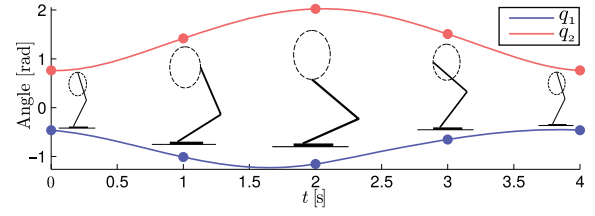


Fig. 10. One period of the joint references.

the Harmonic Drive transmission ratio, consists of the *PB* torques, estimated from the measured deflections: $\hat{\tau}_{PB} = K_{PB} (\theta_1 - \mathbf{q})$ where $\hat{[\cdot]}$ denotes the estimated variables, since we neglect the damping components.

B. Pretension Control

Recalling (13) and solving for p , we can calculate the pretension position p_{opt} that achieves a desired monoarticulated *ESB* torque τ_m^* given the joint position q . This results in

$$p_{opt} = r q + \eta_2 \tau_m^* \quad (27)$$

where $\eta_2 = (r k_p)^{-1}$. In the biarticulated case (15) with a driven joint i , spanned joint j and desired driven joint torque $\tau_{b,i}^*$ this results in

$$p_{opt,i} = r_{b,i} q_i + r_{b,j} q_j + \eta_{2,i} \tau_{b,i}^* \quad (28)$$

where $\eta_{2,i} = (r_{b,i} k_{p,i})^{-1}$ denotes the pulley radius and *ESB* stiffness parameters for the driven joint. Using (27) and (28), we construct the vector function $\mathbf{p}_{opt}(\mathbf{q}, \tau_{p,d}^*) \in \mathbb{R}^N$ that calculates the vector of pretension positions that produce desired *ESB* torques for our chosen actuator configuration.

As noted before, we choose to track the low-frequency components of each element of \mathbf{p}_{opt} . We write this as $\tilde{\mathbf{p}}_{opt}$, where $\tilde{[\cdot]}$ denotes low-pass filtering. This structure ensures that in steady state $\tilde{\mathbf{p}}_{opt} \rightarrow \mathbf{p}_{opt}$, such that $\tau_p \rightarrow \tau^*$ which means all torque is generated by the *ESBs*, resulting in the most energy efficient steady-state operation. The low-pass filters (*LPF* blocks in Fig. 9) have a cut-off frequency of 0.03 Hz. To avoid slack in the compliant elements due to lag resulting from filtering, we calculate zero pretension positions (positions where $\Delta L_p = 0$ for all *ESBs*) as $\mathbf{p}_{zp}(\mathbf{q}) = \mathbf{p}_{opt}(\mathbf{0}, \mathbf{q})$, and define the vector of pretension reference positions $\mathbf{p}^* = [p_1^*, \dots, p_N^*]^T \in \mathbb{R}^N$ as

$$p_i^* = \max(\tilde{p}_{opt,i}, p_{zp,i}), \quad i = 1 \dots N. \quad (29)$$

The pretension positions are then controlled by applying position control with compensation (red block in Fig. 9):

$$\tau_{M2}^* = \eta_3^{-1} \tau_p + K_p [\mathbf{e}_p + D_p \dot{\mathbf{e}}_p] \quad (30)$$

where $\mathbf{e}_p = \mathbf{p}^* - \mathbf{p} \in \mathbb{R}^N$ denotes the pretension position errors, and $K_p, D_p \in \mathbb{R}^{N \times N}$ denote diagonal control gain matrices. The compensation term $\eta_3^{-1} \tau_p$ consists of the measured *ESB* torques reflected to the motors, where the diagonal matrix $\eta_3 \in \mathbb{R}^{N \times N}$ denotes the transmission ratios from *ESB* torque to *M2* motor torque.

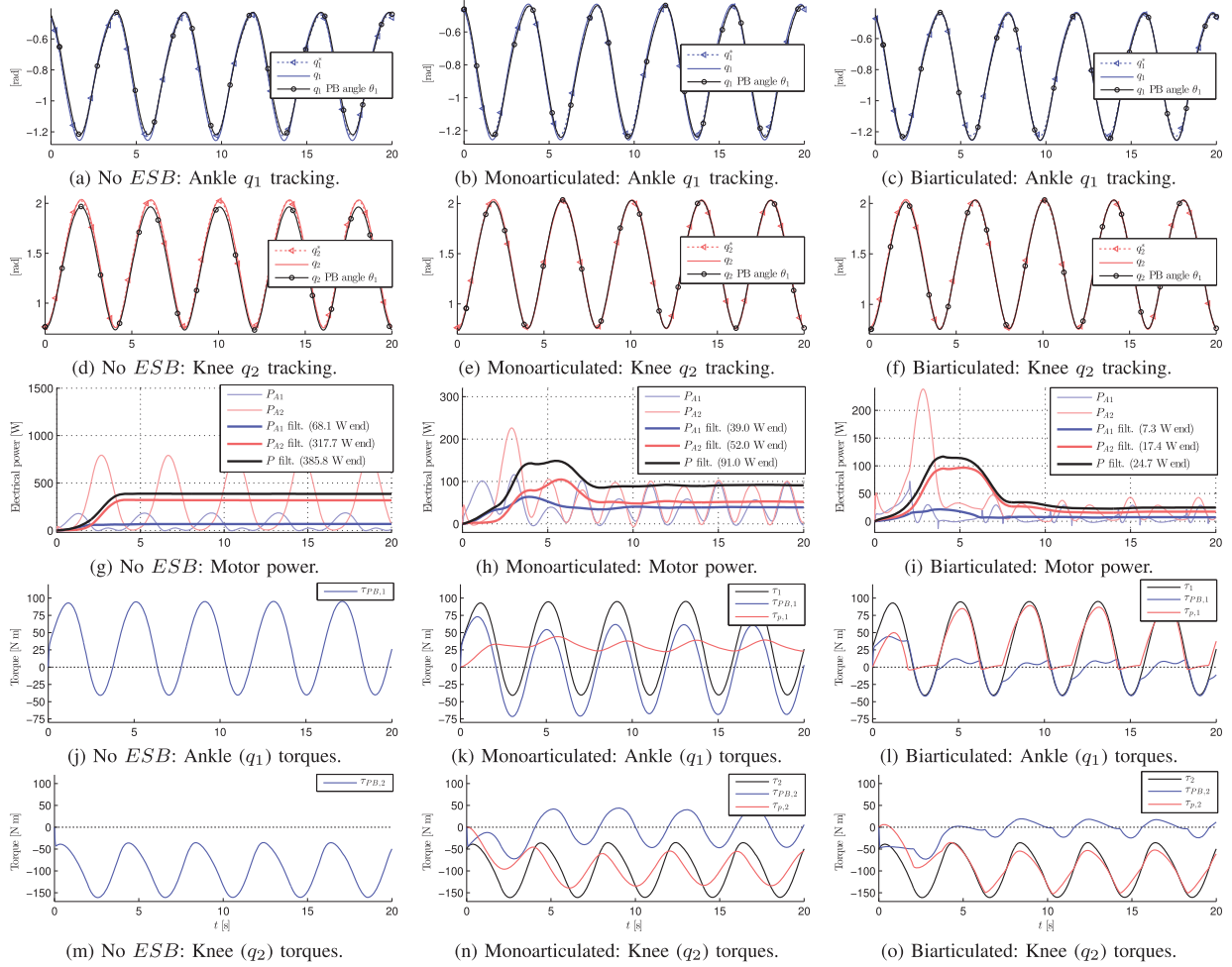


Fig. 11. Simulation results. Left column: without *ESB* (conventional SEA), middle column: monoarticulated configuration, right column: biarticulated configuration. The *filt.* variables denote averages over the period ($2\pi/\omega = 4.0$ s)

V. RESULTS

We performed simulation studies to systematically analyse the effectiveness of the proposed design and control methods in Sec. III–IV. We compare the three actuation configurations discussed in Sec. III–C, by performing an ellipsoid motion (Fig. 10) with the hip above the foot, to effectively utilise the range of motion of this 2-DoF system.

The hip reference position is given by

$$\begin{bmatrix} x_{hip}(t) \\ y_{hip}(t) \end{bmatrix} = \begin{bmatrix} \alpha_x \sin(\omega t) + \beta_x \\ \alpha_y \sin(\omega t + \pi/2) + \beta_y \end{bmatrix}, \quad (31)$$

where $\alpha_x = 0.3l$ m, $\alpha_y = 0.4l$ m, $\omega = \pi/2$ rad/s, $\beta_x = 0.15l$ m, and $\beta_y = 1.45l$ m. We use electrical energy consumption as our energy efficiency metric, since this is often the factor that limits the autonomous operation of mobile robotic systems due to battery constraints. We do so by calculating the total (*PB* + *ESB*) actuator power of ankle (P_{A1}) and knee (P_{A2}), as well as their sum P .

1) *No ESB*: In the conventional SEA configuration we observe a total electrical power consumption of 385.8 W, most of which is used by the knee actuator (Fig. 11g), due to very large gravitational load containing a large DC component of ≈ 100 Nm, as observed in Fig. 11m.

2) *Monoarticulated Configuration*: In the monoarticulated configuration, the gravitational loading is largely compensated by the *ESBs* (Fig. 11k, 11n). The torque generated by the *PBs* converges to a zero mean, demonstrating the DC component is completely generated by the *ESBs*. This results in improved tracking performance and an electrical power consumption of 91.0 W (Fig. 11h), approximately 4 times smaller than without *ESB*.

3) *Biarticulated Configuration*: The biarticulated actuation utilises the *ESBs* to generate the desired torques to an even larger extent. The biarticulated *ESB* extends by both knee extension and dorsiflexion. Thus, moving the hip forward and extending the leg naturally generates torque on the ankle, as observed in Fig. 11l, where the ankle torque is generated to a greater extent by the biarticulated *ESB* compared to the monoarticulated case. Due to the unidirectionality of *ESBs*, the negative joint torques are generated by the *PB*. Furthermore, the contribution of the combined *ESB* torques on the knee is also increased compared to the monoarticulated case, as observed in Fig. 11o.

This human-inspired configuration demonstrates further reduced electrical power consumption of 24.7 W (Fig. 11i), over 15x smaller than without *ESB* and 3.7x smaller than the

monoarticulated configuration. In both cases, the peak power requirements are also significantly reduced.

As additional verification, we studied randomly generated motions. Compared to SEA, the monoarticulated and biarticulated cases were 4–10x and 10–25x more energy efficient, respectively.

VI. CONCLUSIONS & FUTURE WORK

In this letter, the design concepts and control structure of our asymmetric compliant actuator (ACA) concept were generalised and extended to multi-DoF robotic systems. Furthermore, the concept of biarticulated actuation structures was explored as an alternative to purely monoarticulated configurations.

Extensive simulation studies of our methods on a 2-DoF leg as proof of concept effectively demonstrated significant improvements in energy efficiency and tracking accuracy, compared against conventional series-elastic actuation found on many robotics systems. Notably, compared to SEA, the monoarticulated case required 4–10x less energy and the biarticulated case required over 10–25x less energy. Furthermore, peak electrical power requirements were greatly reduced.

The addition of a secondary actuation branch requires additional components; however, these secondary components can be implemented in a small and lightweight manner due to the high transmission ratio. The increase in energy efficiency greatly offsets the small increase in weight and complexity. Given these very promising results we believe the ACA concept can contribute to improved energy efficiency of many systems in the robotics field.

The work presented in this letter provides the necessary guidelines to build new hardware that utilises these concepts. Future work will focus on improvements to the control architecture and integration with the WALK-MAN humanoid.

REFERENCES

- [1] A. Jafari, N. G. Tsagarakis, and D. G. Caldwell, "Exploiting natural dynamics for energy minimization using an actuator with adjustable stiffness (AWAS)," in *Proc. IEEE Int. Conf. Robot. Autom. (ICRA)*, 2011, pp. 4632–4637.
- [2] B. Vanderborght, N. G. Tsagarakis, R. Van Ham, I. Thorson, and D. G. Caldwell, "MACCEPA 2.0: Compliant actuator used for energy efficient hopping robot chobino1d," *Auton. Robots*, vol. 31, no. 1, pp. 55–65, 2011.
- [3] G. Mathijssen, D. Lefeber, and B. Vanderborght, "Variable recruitment of parallel elastic elements: Series-parallel elastic actuators (SPEA) with dephased mutilated gears," *IEEE/ASME Trans. Mechatron.*, vol. 20, no. 2, pp. 594–602, Apr. 2014.
- [4] A. Velasco, G. M. Gasparri, M. Garabini, L. Malagia, P. Salaris, and A. Bicchi, "Soft-actuators in cyclic motion: Analytical optimization of stiffness and pre-load," in *Proc. 13th IEEE-RAS Int. Conf. Humanoid Robots (Humanoids)*, 2013, pp. 354–361.
- [5] M. Garabini, A. Passaglia, F. Belo, P. Salaris, and A. Bicchi, "Optimality principles in stiffness control: The VSA kick," in *Proc. IEEE Int. Conf. Robot. Autom. (ICRA)*, 2012, pp. 3341–3346.
- [6] K. Kong, J. Bae, and M. Tomizuka, "Control of rotary series elastic actuator for ideal force-mode actuation in human—Robot interaction applications," *IEEE/ASME Trans. Mechatron.*, vol. 14, no. 1, pp. 105–118, Feb. 2009.
- [7] C. Ott, A. Albu-Schaffer, A. Kugi, and G. Hirzinger, "On the passivity-based impedance control of flexible joint robots," *IEEE Trans. Robot.*, vol. 24, no. 2, pp. 416–429, Apr. 2008.
- [8] N. Paine, S. Oh, and L. Sentis, "Design and control considerations for high-performance series elastic actuators," *IEEE/ASME Trans. Mechatron.*, vol. 19, no. 3, pp. 1080–1091, Jun. 2014.
- [9] A. Bicchi, G. Tonietti, M. Bavaro, and M. Piccigallo, "Variable stiffness actuators for fast and safe motion control," in *Proc. Int. Symp. Robot. Res.*, 2003, pp. 100–110.
- [10] M. Laffranchi, N. G. Tsagarakis, and D. G. Caldwell, "Safe human robot interaction via energy regulation control," in *Proc. IEEE/RSJ Int. Conf. Intell. Robots Syst. (IROS)*, 2009, pp. 35–41.
- [11] R. Schiavi, G. Grioli, S. Sen, and A. Bicchi, "VSA-II: A novel prototype of variable stiffness actuator for safe and performing robots interacting with humans," in *Proc. IEEE Int. Conf. Robot. Autom. (ICRA)*, 2008, pp. 2171–2176.
- [12] S. Shirata, A. Konno, and M. Uchiyama, "Design and evaluation of a gravity compensation mechanism for a humanoid robot," in *Proc. IEEE/RSJ Int. Conf. Intell. Robots Syst. (IROS)*, 2007, pp. 3635–3640.
- [13] G. A. Pratt and M. Williamson, "Series elastic actuators," in *Proc. IEEE Int. Workshop Intell. Robots Syst. (IROS)*, 1995, pp. 399–406.
- [14] R. Van Ham, B. Vanderborght, M. Van Damme, B. Verrelst, and D. Lefeber, "Macepa, the mechanically adjustable compliance and controllabel equilibrium position actuator: Design and implementation in a biped robot," *Robot. Auton. Syst.*, vol. 55, no. 10, pp. 761–768, 2007.
- [15] B. Vanderborght, N. G. Tsagarakis, C. Semini, R. Van Ham, and D. G. Caldwell, "Macepa 2.0: Adjustable compliant actuator with stiffening characteristic for energy efficient hopping," in *Proc. IEEE Int. Conf. Robot. Autom. (ICRA)*, 2009, pp. 544–549.
- [16] S. Wolf, O. Eiberger, and G. Hirzinger, "The DLR FSJ: Energy based design of a variable stiffness joint," in *Proc. IEEE Int. Conf. Robot. Autom. (ICRA)*, 2011, pp. 5082–5089.
- [17] S. S. Groothuis, G. Rusticelli, A. Zucchelli, S. Stramigioli, and R. Carloni, "The variable stiffness actuator vsaUT-II: Mechanical design, modeling, and identification," *IEEE/ASME Trans. Mechatron.*, vol. 19, no. 2, pp. 589–597, Apr. 2014.
- [18] A. Jafari, N. G. Tsagarakis, I. Sardellitti, and D. G. Caldwell, "A new actuator with adjustable stiffness based on a variable ratio lever mechanism," *IEEE/ASME Trans. Mechatron.*, vol. 19, no. 1, pp. 55–63, Feb. 2014.
- [19] G. J. V. I. Schenau, "From rotation to translation: Constraints on multi-joint movements and the unique action of bi-articular muscles," *Hum. Mov. Sci.*, vol. 8, no. 4, pp. 301–337, 1989.
- [20] I. Prilutsky and V. M. Zatsiorsky, "Tendon action of two-joint muscles: Transfer of mechanical energy between joints during jumping, landing, and running," *J. Biomech.*, vol. 27, no. 1, pp. 25–34, 1994.
- [21] R. Niiyama, A. Nagakubo, and Y. Kuniyoshi, "Mowgli: A bipedal jumping and landing robot with an artificial musculoskeletal system," in *Proc. IEEE Int. Conf. Robot. Autom. (ICRA)*, 2007, pp. 2546–2551.
- [22] J. Babic, B. Lim, D. Omrcen, J. Lenarcic, and F. C. Park, "A biarticulated robotic leg for jumping movements: Theory and experiments," *J. Mech. Robot.*, vol. 1, no. 1, p. 11–13, 2009.
- [23] T. J. Klein and M. A. Lewis, "A robot leg based on mammalian muscle architecture," in *Proc. IEEE Int. Conf. Robot. Biomimetics (ROBIO)*, 2009, pp. 2521–2526.
- [24] V. Salvucci, Y. Kimura, S. Oh, T. Koseki, and Y. Hori, "Comparing approaches for actuator redundancy resolution in biarticularly-actuated robot arms," *IEEE/ASME Trans. Mechatron.*, vol. 19, no. 2, pp. 765–776, Apr. 2014.
- [25] F. Iida, J. Rummel, and A. Seyfarth, "Bipedal walking and running with spring-like biarticular muscles," *J. Biomech.*, vol. 41, no. 3, pp. 656–667, Jan. 2008.
- [26] N. Tsagarakis, S. Morfeý, G. M. Cerda, H. Dallali, and D. G. Caldwell, "An asymmetric compliant antagonistic joint design for high performance mobility," in *Proc. IEEE/RSJ Int. Conf. Intell. Robots Syst. (IROS)*, 2013, pp. 5512–5517.
- [27] N. Tsagarakis, H. Dallali, F. Negrello, W. Roozing, G. M. Cerda, and D. G. Caldwell, "Compliant antagonistic joint tuning for gravitational load cancellation and improved efficient mobility," in *Proc. IEEE/RAS Int. Conf. Humanoid Robots*, 2014, pp. 924–929.
- [28] W. Roozing, Z. Li, G. A. Medrano-Cerda, D. G. Caldwell, and N. G. Tsagarakis, "Development and control of a compliant asymmetric antagonistic actuator for energy efficient mobility," *IEEE/ASME Trans. Mechatron.*, 2015, pp. 1–12.
- [29] Italian Institute of Technology. (2015). WALK-MAN [Online]. Available: <http://walk-man.eu/>